Materials Advances

PAPER

Check for updates

Hierarchical α-MnO₂ nanowires as an efficient anode material for rechargeable lithium-ion batteries†

Ediga Umeshbabu, [iD] *[ab] M. Satyanarayana,[c] Guruprakash Karkera, [iD] [b] Ashok Pullamsetty[d] and P. Justin*[e]

In this work, a bulk quantity of α-MnO₂ hierarchical nanowires was synthesized by a facile redox reaction between potassium permanganate (KMnO₄) and glycine under ambient conditions. The physicochemical characterization results revealed that the MnO₂ sample exhibited highly uniform (1D) nanowire morphology and unique surface texture features such as a high specific surface area of 181 m² g⁻¹ with a beneficial mesoporous structure. Taking the advantage of hierarchical 1D nanowires morphology and improved microstructural properties, a cell with MnO₂ nanowires as an anode showed relatively good electrochemical performance with enhanced lithiation degree and improved cycling stability. The initial discharge capacity of as high as 1373 mA h g⁻¹ was achieved at 100 mA g⁻¹ and rendered a reversible capacity of 735 mA h g⁻¹ even after 100 cycles with an average Coulombic efficiency of 97%. The improved electrochemical performance of α-MnO₂ is attributed to its hierarchical nanowire morphology and enriched textural surface properties, which provide a good Li-ion diffusion path, large electrode–electrolyte contact area and effective accommodation of the strain generated from volume expansion during repeated lithiation/delithiation processes.

1. Introduction

Among various kinds of electrochemical energy storage devices, lithium-ion batteries (LIBs) have been extensively used in many electronic applications throughout the past decades as primary sources of power. In recent years, they have been explored as promising candidates for electric vehicle applications due to their advantages of high gravimetric/volumetric energy, high power density, prolonged cycle-life, and low self-discharge properties.[1–4] Traditionally, graphite is used as an anode material in commercial LIBs due to its layered structure that facilitates the Li⁺ ion intercalation effectively. The limited theoretical specific capacity and poor rate capability of graphite

[a] Department of Chemistry, Indian Institute of Technology Madras, Chennai - 600036, India. E-mail: umeshediga@gmail.com

[b] Helmholtz Institute Ulm (HIU) for Electrochemical Energy Storage, Helmholtzstraße 11, D-89081 Ulm, Germany

[c] Department of Chemistry, Faculty of Exact Sciences, Bar-Ilan University, Ramat-Gan 5290002, Israel

[d] Department of Physics, Indian Institute of Technology Madras, Chennai - 600036, India

[e] Department of Chemistry, Rajiv Gandhi University of Knowledge Technologies, RK Valley, Kadapa 516330, Andhra Pradesh, India. E-mail: ponjustin@rgukt.in

† Electronic supplementary information (ESI) available. See DOI: 10.1039/d1ma00755f

are inadequate to power high energy demands for electric vehicle applications.[5] Therefore, it is imperative to develop highly efficient and advanced anode materials in building next-generation Li batteries with high specific capacity and high energy densities, so as to meet the ever-growing performance demands.[3,6–9]

Transition metal oxides (MO$_x$; M = Ni, Co, Fe, Nb, Mo, and so forth)[8–15] have been researched intensively as promising alternative anode materials for LIBs because they are suggested to have extremely high reversible capacities of about three times higher than that of graphite (2–3 times that of graphite) owing to their unique conversion type reactions (MO$_x$ + 2xLi⁺ + 2xe⁻ ↔ M + xLi₂O) and ability to tune the working voltage as well as the energy density by selecting the metal type.[16] Moreover, these oxides are low-cost and environmentally benign. Among metal oxides, MnO₂ is regarded as one of the promising anode material for LIBs due to its inherent advantages such as natural abundance, low-cost, environmental benignity and large theoretical capacity of 1230 mA h g⁻¹.[17–19] In addition, MnO₂ can crystallize in different kinds of polymorphs, *i.e.* α-, β-, γ-, λ- δ- and ε-types, which are connected by the basic unit, [MnO₆] octahedron, by sharing edges or corners. As a result, they possess tunnels or interlayers with gaps of different magnitudes, which provide effective diffusion pathways for Li⁺ ions.[19–23] Among phases, α-MnO₂ shows adequate Li⁺ charge storage ability since

it has a hollandite-type crystal structure with relatively large 1D [2 × 2] tunnels formed *via* interlinked octahedral [MnO$_6$] units, which enable easier and faster ionic transport and electrode reaction kinetics within the MnO$_2$ framework.[24,25] In addition, the hollow-interior structures can minimize the volume expansion during the charging/discharging process. However, several intrinsic problems existing in MnO$_2$ include low electronic conductivity and pulverization of small particles during the Li$^+$ ion insertion/extraction process, which results in poor rate performance and rapid capacity fading during long cycling.[18,26]

In order to relieve the aforementioned inherent difficulties and thereby improve battery performance with good cycling stability, nanotechnology (fabricating MnO$_2$ in nanostructures or hybrid composites with a conductive matrix such as graphene, polymers, *etc.*) has become one of the efficient approach.[18,26–32] The physicochemical and electrochemical properties of MnO$_2$ are significantly influenced by its crystalline structure, morphology and synthetic methods as well as its compositional characteristics. For example, Li *et al.* synthesized hollow-urchin-like MnO$_2$ by a low-temperature mild reduction route, which showed a discharge capacity of 481 mA h g^{-1} after 40 cycles.[27] Chen *et al.* reported MnO$_2$ nanorods using a hydrothermal method that provided a discharge capacity of 930 mA h g^{-1} after 100 cycles.[28] A coaxial MnO$_2$/carbon nanotube array was reported by Reddy *et al.* fabricated using a chemical vapor deposition (CVD) technique and the hybrid electrode material delivered a very high initial capacity of 2000 mA h g^{-1} at 50 mA g^{-1}; however, the discharge capacity faded very fast with only 500 mA h g^{-1}, about 25% of the initial capacity at 15th cycle.[31] Nonetheless, such methods have multitudinous shortfalls, such as complex time-intensive steps and high equipment costs. Indeed, some of the methods, mainly the utilization of CVD gets lower yield. Therefore, developing MnO$_2$ nanomaterials through simple, environmentally-friendly and cost-effective methods are imperative.

In this work, we employed a simple, inexpensive and straightforward approach to synthesize hierarchical α-MnO$_2$ nanowires through a reaction involving KMnO$_4$ and glycine. This approach involves simple mixing of the precursors in the solution medium and subsequent annealing. Moreover, glycine is a non-toxic, biodegradable and relatively cheap amino acid whose amino group can effectively undergo ionic interaction with Mn^{7+} ions and reduce KMnO$_4$ successfully to produce MnO$_2$ at room temperature.[33] The combined physicochemical and electrochemical measurements were performed on the MnO$_2$ sample to scrutinize the structural and charge/discharge performance. The prepared material exhibits α-phase and hierarchical 1D-nanowire morphology with high specific surface area and incumbent porous structure, which is promising in providing inflated conductive networks with intimate electrode–electrolyte contact and short diffusion lengths for Li$^+$ ions during charge/discharge. Benefiting from such a nanoarchitecture, the α-MnO$_2$ electrode showed a high reversible capacity, excellent cycling stability of over 100 cycles and high rate capability.

2. Experimental section

2.1 Synthesis of α-MnO$_2$ nanowires

All chemical reagents used in this study were of analytical grade and were used without any further purification. α-MnO$_2$ nanowires were prepared by a simple and straightforward *in situ* redox reaction followed by a heat-treatment. In a typical reaction, 5 mmol of solid KMnO$_4$ crystals were dissolved in 100 mL of deionized (DI) water under vigorous magnetic stirring until a transparent purple color solution appeared. To this, 5 mmol of glycine (amino acid and commonly used as a reducing agent) was separately dissolved in 25 mL DI water was added slowly under vigorous magnetic stirring. The total solution mixture was stirred for another 3 h. The purple-colored KMnO$_4$ solution gradually changed to dark brown residue due to the *in situ* redox reaction between permanganate and glycine. The obtained precipitate was centrifuged, washed extensively with copious amounts of DI water followed by washing with absolute ethanol to eliminate the unreacted reactants if any. The collected residue was air-dried overnight, and then calcined in a muffle furnace at 400 °C for 3 h at a ramp rate of 5 °C min^{-1} in the air to engender well-crystalline α-MnO$_2$ nanowires.

2.2 Materials characterization

Thermogravimetric analysis (TGA) and differential thermal analysis (DTA) were performed using a TA make TGA Q500V20.10 Build 36 instrument. For TGA/DTA measurement, the sample was heated from room temperature to 750 °C at a ramp rate of 20 °C min^{-1} in air. XRD was performed on a Bruker AXS D8 advanced diffractometer, using Cu Kα radiation (λ = 1.5418 Å). The phase and lattice constants were identified by Rietveld refinement analysis using the General Structure Analysis System (GSAS) software. A Horiba HR 800UV Raman spectrometer was used with a laser excitation of 632.8 nm to obtain the Raman spectrum. The surface area and pore-size distribution of the sample were obtained using BET (Brunauer–Emmett–Teller) and BJH (Barret–Joyner–Halenda) methods from the data collected on a Micromeritics ASAP 2020 physisorption tool. The microstructure and morphology of the sample were characterized using field emission scanning electron microscopy (FESEM; FEI, Quanta 400). TEM and high-resolution TEM images were obtained using a JEOL JEM 3010 instrument. Prior to TEM measurements, the sample powder was suspended in ethanol by sonication for 5 min and then dispersed on a carbon-coated Cu grid. X-ray photoelectron spectroscopy (XPS) measurements were performed on a PHOIBOS 150 XPS (SPECS-Surface concept) spectrometer with an exciting source of Al Kα = 1486.6 eV. The spectral data were calibrated to 284.6 eV (C 1s).

2.3 Electrochemical measurements

The electrochemical properties were measured using galvanostatic charge/discharge (GCD), cyclic voltammetry (CV) and AC impedance spectroscopy in assembled CR2016-type coin cells. The working electrodes were fabricated by mixing 75 wt% α-MnO$_2$ nanowires, 15 wt% acetylene black, and 10 wt% PVDF

(polyvinylidene fluoride) binder in a ball-milled with the required amount of N-methyl-2-pyrrolidone (NMP) solvent to form a homogeneous slurry. Subsequently, the slurry was painted over a Cu foil current collector using a doctor blade. Then, the electrodes were dried in a vacuum oven at 80 °C and then punched into disks to meliorate the contact among copper foil, active materials, and conductive carbon. The active material loading on each electrodes was 2.0 mg cm^{-2}. Preliminary cell tests were performed using a CR2025 type coin cell with Li metal as the anode and a Celgard 2500 polypropylene separator. The electrolyte solution was 1 M LiPF$_6$ in a 1:1 volume ratio of EC and DMC. The coin cells were assembled in an Ar-filled glove box (O$_2$ and H$_2$O < 0.1 ppm). The cell's discharge–charge cycling was between 0.05 and 3.0 V (vs. Li$^+$/Li) and was conducted on a LAND battery testing system. Cyclic voltammetry (0.005–3.0 V, 1 mV s^{-1}) and impedance spectroscopy (from 0.1 Hz to 1 MHz) were performed on a Versa-STAT (Princeton Applied Research) electrochemical work station. All electrochemical studies were conducted at room temperature.
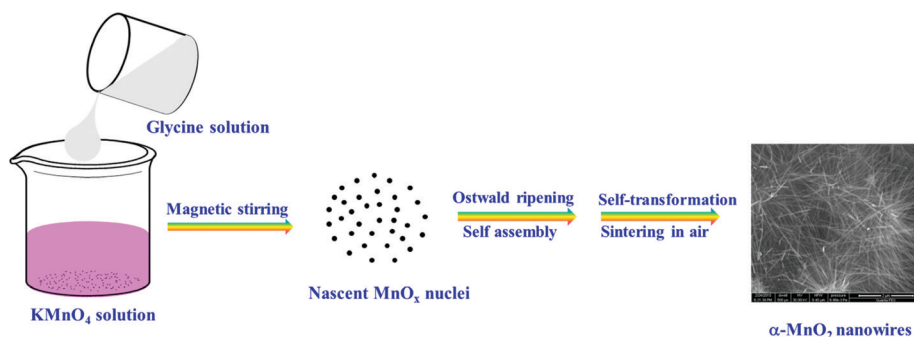
3. Results and discussion

3.1 Morphology and structural characterization

The schematic illustration for the growth mechanism of α-MnO$_2$ 1D nanowires under a solution-processed redox-reaction is shown in Scheme 1. The morphology and crystalline evolution of α-MnO$_2$ nanowires typically involve (i) nucleation of nascent MnO$_x$ nuclei through the reduction between permanganate MnO$_4$$^-$ and glycine, (ii) progression to nanosized particles, (iii) Ostwald ripening and self-assembling and (iv) expeditious self-transformation to hierarchical nanowires under high-temperature calcination.[34,35] The morphology of the uncalcined precursor showed an irregular agglomerated surface structure (Fig. S1A, ESI†). On heat treatment, the agglomerated surface structure transformed into well-defined 1D nanowires of lengths of tens of micrometers and a diameter of 15–25 nm. This unique nanowire morphology can provide better electrochemical accessibility to Li$^+$ ions, leading to better performance towards charge storage characteristics. During the growth process of nanowires, several intrinsic and extrinsic forces and other parameters influence the shape,

orientations, growth of crystallites and the final morphology of oxide.[21,35–37]

To monitor the thermal stability and phase evaluation of the as-prepared MnO$_x$ precursor, we performed thermogravimetric (TGA) and differential thermal analysis (DTA) and the respective patterns are shown in Fig. 1. The TGA profile shows a total weight loss of 16.16% up to a temperature of 470 °C. A steep decrease in weight loss up to 200 °C corresponded to the removal of surface-adsorbed as well as uncoordinated interlayer water and then gradual weight loss from 200 to 470 °C corresponding to the loss of water molecules from the tunnel cavity.[38–40] A small weight (0.71%) increment was observed in the sample at 506 °C due to the compensation of released oxygen produced by the oxidation of subvalent Mn cations to Mn(ıv) leading to the phase transformation from the layered structure to tetragonal the α-MnO$_2$ phase.[40–42] Moreover, the weight loss observed at about 665 °C, corresponds to the phase transformation of MnO$_2$ to Mn$_2$O$_3$.[39,41] The XRD pattern of the uncalcined precursor in Fig. S1B (ESI†) exhibits broad diffraction peaks at about 12°, 25°, 37.2° and 66.2°, which can be indexed to amorphous MnO$_2$ phase with poorly crystalline nature.[43]

The crystal structure of α-MnO$_2$, as shown in Fig. 2A and B encompass double chains of the edge-shared MO$_6$ octahedra, which are interconnected at corners to form (2 × 2) and (1 × 1) tunnels in the tetragonal unit cell. The XRD pattern and Rietveld refinement affirmed the phase purity and lattice structure of the prepared MnO$_2$. Rietveld refinement of XRD patterns was executed by the General Structure Analysis System (GSAS) and corresponding results are depicted in Fig. 2C. All reflections in the XRD pattern can be indexed to the tetragonal α-MnO$_2$ with a space group I4/m (JCPDS no# 42-1348). Importantly, we did not find any impurity peaks in the XRD pattern, signifying that the as-prepared α-MnO$_2$ sample is a pure phase.[21] The better χ^2 (~2.1) reveals that the Rietveld refinement exercise is a good fit with the experimental data. R_p and R_{wp} values are 3.9% and 5.4%, respectively. The refined lattice constants are $a = b = 9.842$ Å and $c = 2.858$ Å, which are consistent with the literature values of $a = b = 9.871$ Å and $c = 2.858$ Å.[44] Further, the average crystallite size of α-MnO$_2$ was calculated to be 15.3 nm using Scherrer's equation.[21] Raman spectrum of α-MnO$_2$, as shown in Fig. 3, unveils well-resolved

Scheme 1 A Schematic illustration for the formation process of α-MnO$_2$ nanowires under a solution-processed redox-reaction between permanganate and glycine.
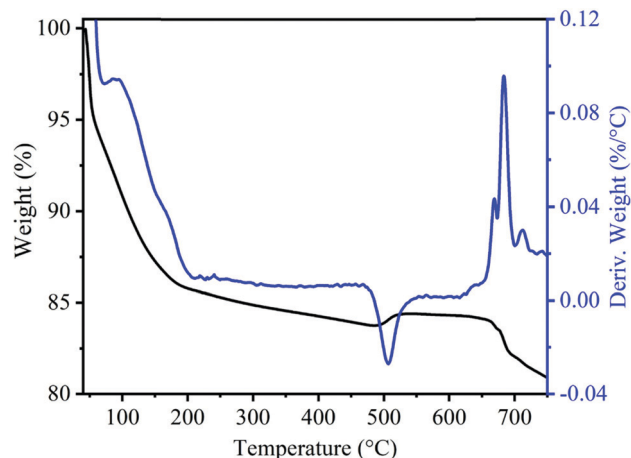
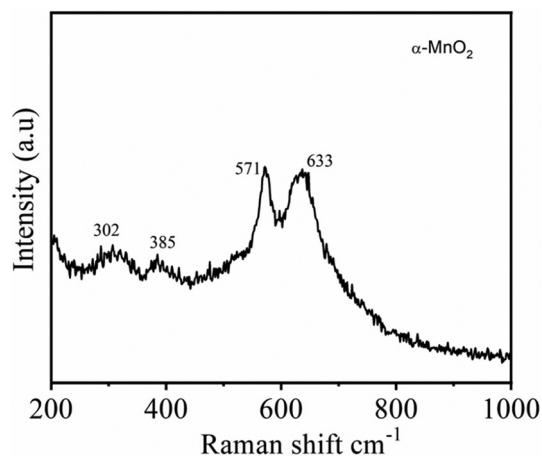**Fig. 1** TGA and DTG curves of uncalcined precursors of MnO_2 sample.

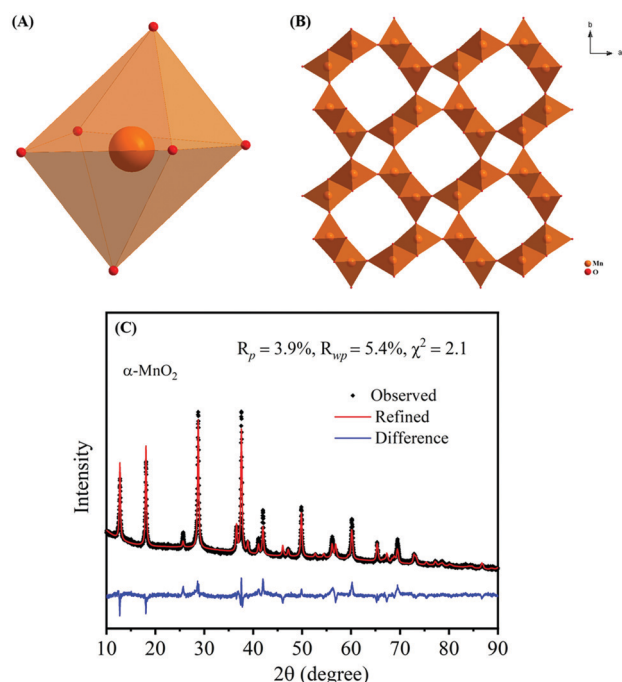**Fig. 3** Raman spectra of the α-MnO_2 nanowires.

Fig. 2 Crystallographic structures of α-MnO_2: (A) MnO_6 octahedron structural unit and (B) α-MnO_2 (2 × 2 tunnels); (C) X-ray Rietveld refinement results of the α-MnO_2 sample.

Raman bands located at 302, 385, 571 and 633 cm^{-1} that are characteristic of the α-MnO_2 phase.[45,46] It is worth noting that all materials with the α-MnO_2 crystal phase reported two diagnostic peaks at around 571 and 633 cm^{-1}. The former peak is the M–O stretching vibration in the basal plane of the MnO_6 sheet, while the latter corresponds to the M–O symmetric stretching vibration of the MnO_6 groups.[26,46]

To inspect the morphology and microstructure of the prepared α-MnO_2, scanning electron microscopy and transmission electron microscopy were performed and the corresponding results are shown in Fig. 4 and 5, respectively. From the low-magnification

SEM images (Fig. 4A and B), the MnO_2 sample shows hierarchical ultralong 1D nanowires morphology. The high-magnification SEM in Fig. 4C and D unveils the nanowire's lengths as tens of micrometers and their widths in the range of 15–25 nm. The representative TEM images (Fig. 5A and B) of the MnO_2 sample revealed the distribution of nanowires evenly and the average diameter of nanowires as 20 nm. The high-resolution TEM pictures (Fig. 5C–E) display clear lattice fringes with an interplanar spacing between neighboring lattice fringes as 0.685, 0.501, 0.315 and 0.245 nm, all of which are in good agreement with XRD results of (110), (200), (310) and (211) planes of α-MnO_2 (JCPDS# 42-1348). The selected area electron diffraction (SAED) pattern (Fig. 5F), reveals typical concentric circles, suggesting the polycrystalline nature of α-MnO_2 nanowires.

To measure the surface textural characteristics of α-MnO_2 nanowires, we collected nitrogen adsorption and desorption
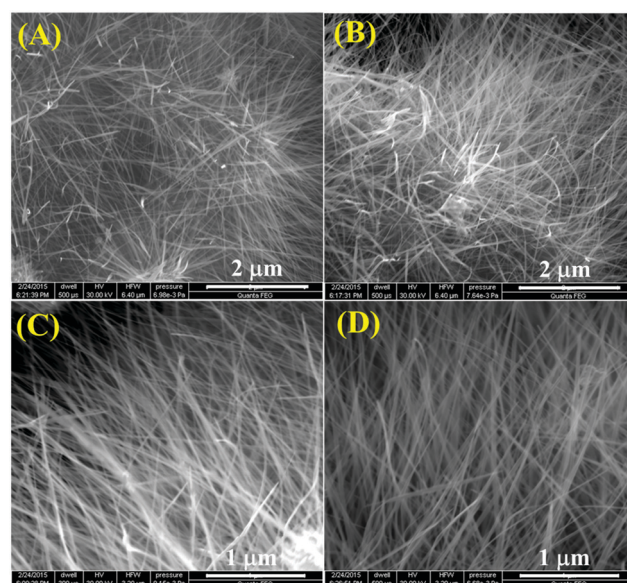

Fig. 4 (A–D) Field emission scanning electron microscopy (FESEM) images of the α-MnO_2 sample at different magnifications.
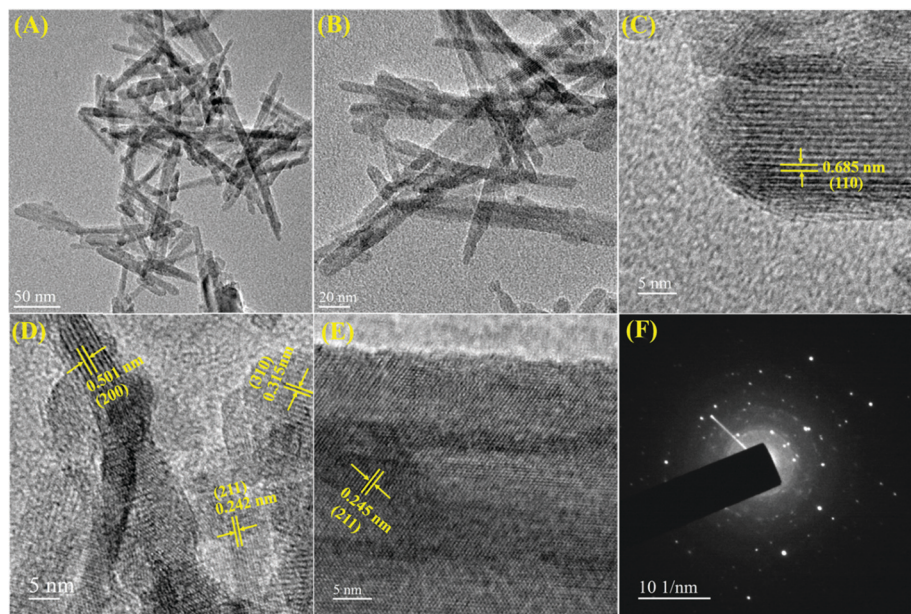
Fig. 5 Different magnified (A and B) TEM images and (C−E) high-resolution TEM images of the α-MnO$_2$ sample; (F) SAED pattern of the corresponding sample.

isotherms (Fig. 6) on the material. As seen in Fig. 6A, the isotherms have type-IV characteristics (based on IUPAC classification) with a capillary condensation step viewing at high relative pressures (P/P_0) between 0.4 and 0.9 that distinctly signifies mesoporous nature of the MnO$_2$ sample. The pore distribution profile (Fig. 6B) further revealed a unimodal pore-size distribution with a pore maximum of 2.96 nm. The estimated specific surface area and pore volume of α-MnO$_2$ nanowires are 181 m^2 g^{-1} and 0.257 cm^3 g^{-1}, respectively. We note that the specific surface area of our α-MnO$_2$ nanowires is far away from others reported in literature prepared by a different method such as hollow-urchins (132 m^2 g^{-1}),[27] nanopetals (68 m^2 g^{-1}),[17] nitrogen-enriched porous carbon–MnO$_x$ hybrid (148 m^2 g^{-1})[4] and MnO$_2$–polythiophene (136 m^2 g^{-1}).[32] It has commonly been reported that the electrode materials comprising high specific surface area and large pore-volume as well as the indispensable mesoporous structure could reinforce the electrode–

electrolyte contact and afford a facile e$^-$ transport as well as a short path for Li$^+$ diffusion during charge/discharge process.[47,48] Therefore, we expected, α-MnO$_2$ featuring hierarchical 1D nanowires morphology and favorable textural properties would provide the possibility of efficient transport of electrolyte ions in Li-ion batteries.

The elemental composition and their valence state of Mn ions in α-MnO$_2$ nanowires were investigated using the X-ray photoelectron spectroscopy technique. Fig. 7A shows the XPS survey scan, demonstrating the presence of Mn and O as well as C from the reference. It also confirms the absence of any apparent impurities in the prepared sample. The high-resolution Mn 2p spectrum (Fig. 7B) shows a spin–orbit doublet with binding energy peaks at 642.3 eV (Mn 2p$_{1/2}$) for and 654.15 eV for (Mn 2p$_{3/2}$), suggesting that the oxidation state of Mn is 4+.[49] In the high-resolution O 1s spectrum (Fig. 7C), the peaks located
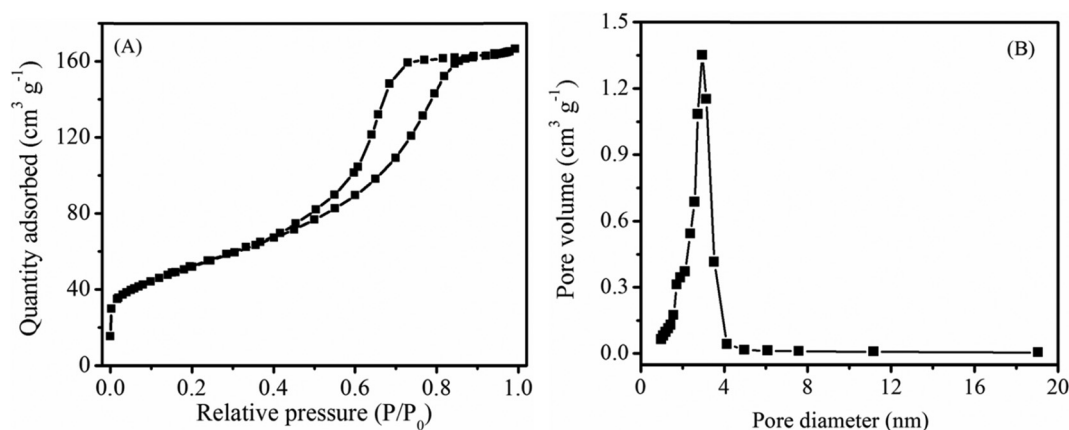

Fig. 6 (A) N$_2$ adsorption−desorption isotherms and (B) BJH pore-size distribution profile of the α-MnO$_2$ sample.
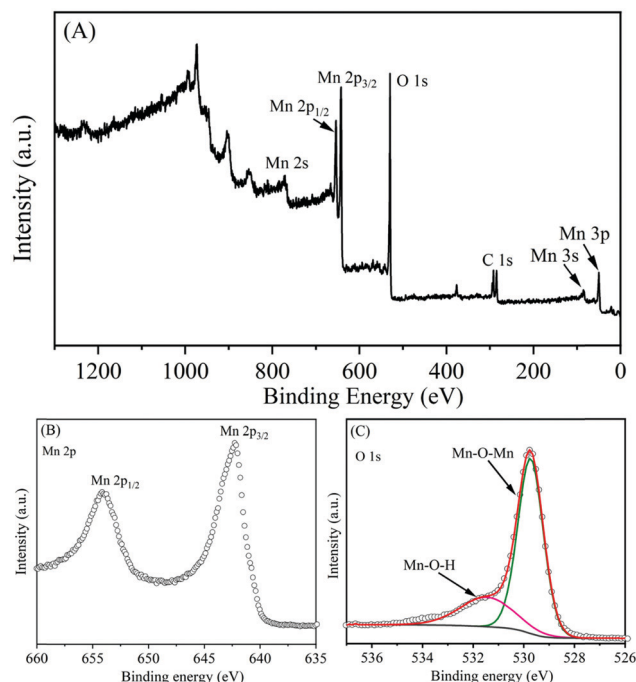
Fig. 7 (A) XPS survey spectrum of α-MnO$_2$; core-level XPS of (B) Mn 2p and (C) O 1s.

at binding energies of 529.75 eV and 531.50 eV, which correspond to those for anhydrous (Mn–O–Mn) and hydrated (Mn–O–H) manganese oxides, respectively.[50,51]

3.2 Electrochemical performance

To investigate the electrochemical properties of as-prepared α-MnO$_2$ nanowires as anodes for LIBs in the half-cell configuration, cyclic voltammograms and galvanostatic discharge–charge cycling tests were performed. Fig. 8 shows typical CV profiles of tα-MnO$_2$ nanowires obtained at a 0.1 mV s^{-1} scan rate within a voltage range of 0.005–3.0 V (vs. Li/Li$^+$). Generally, the reaction between transition metal oxides (e.g., MnO$_2$) and Li is typically a conversion-type
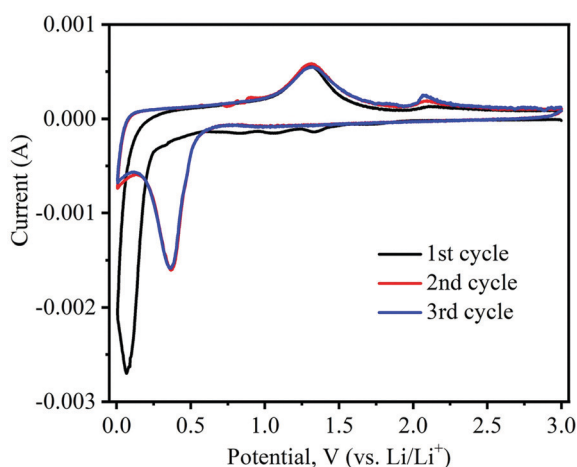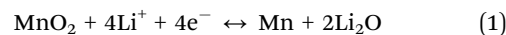

Fig. 8 Cyclic voltammetry (CV) curves of α-MnO$_2$ nanowires electrode recorded at a sweep rate of 0.1 mV s^{-1} and 0.05–3.0 V (vs. Li/Li$^+$) potential range.

mechanism.[52] The CV profiles of α-MnO$_2$ nanowires are consistent with those reported for relevant systems,[53–56] demonstrating a similar Li storage mechanism is taking place in our system, which is as follows:

$$MnO_2 + 4Li^+ + 4e^- \leftrightarrow Mn + 2Li_2O \qquad (1)$$

Noticeably, the CV shape of the first cathodic curve essentially contrasts with the posterior ones. Upon the first scan in the cathodic (lithiation) process, the prominent irreversible peaks are situated at 1.34 and 1.06 V, caused by electrolyte decomposition leading to the solid electrolyte interphase (SEI) formation on electrode surfaces.[52] A small peak appears at 0.84 V, which corresponds to the reduction of Mn^{4+} to Mn^{2+}.[55,56] The large intensity peak at approximately 0.07 V during the first cycle can be imputed to the reduction of Mn^{2+} to Mn^0.[54,57] In the following delithiation (anodic) process, two distinctive peaks are noticed at 1.31 and 2.08 V, indicating that reversible oxidation of metallic Mn (i.e., Mn^0 to Mn^{2+} and Mn^{2+} to Mn^{4+}, respectively).[28,54] Interestingly, in the subsequent second and third cycles of the cathodic process, peak position shifts from 0.07 V to 0.36 V, which can be attributed to the structural reconstruction resulting from the formation of Li$_2$O and manganese metal through the conversion reaction, as shown in eqn (1).[52] In the second and third anodic cycles, the peaks' positions were almost identical to those in the first one (1.31 and 2.08 V).

The galvanostatic charge/discharge experiment within a voltage range of 0.05–3.0 V (vs. Li/Li$^+$) was employed to further investigate the electrochemical lithiation/delithiation process of the as-prepared α-MnO$_2$ nanowire electrode. The active material loading was 2.0 mg cm^{-2}. The specific capacity of the cells was estimated from the loading of the active material. Fig. 9A shows typical charge/discharge characteristics (i.e., voltage vs. capacity) of α-MnO$_2$ nanowire electrode at a specific current of 100 mA g^{-1}. During the charge and discharge process, noticeable plateaus at 1.0 and 0.4 V are observed, consistent with literature reports,[55,58] suggesting similar lithium intercalation/absorption behaviour occurring in α-MnO$_2$ nanowires. The cell's 1st discharge and charge capacities are 1373 and 852 mA h g^{-1}, respectively, leading to a relatively low Coulombic efficiency of 62%. The discharge capacities for the subsequent cycles (2nd to 10th) are 897, 878, 851, 846, 837, 833, 837, 834 and 836 mA h g^{-1}, respectively. The abnormal high capacity during the 1st discharge is caused by electrolyte decomposition and the inevitable formation of the SEI passivation layer, which is common in most anode materials.[54,56]

The long-term cycling stability is also an important parameter and was measured to determine the strength of the electrode. The galvanostatic charge–discharge technique was employed to evaluate the cycling stability of the α-MnO$_2$ electrode at a current density of 100 mA g^{-1} in a potential window of 0.05 and 3.0 V. Fig. 9B illustrates the 1st to 100th charge/discharge profiles of α-MnO$_2$ at an applied current of 100 mA g^{-1}. The profiles show a stable performance upon increasing the cycle number up to 100 cycles. As seen from Fig. 9C, the capacity of the cells decreased gradually with cycle number. Remarkably, a high
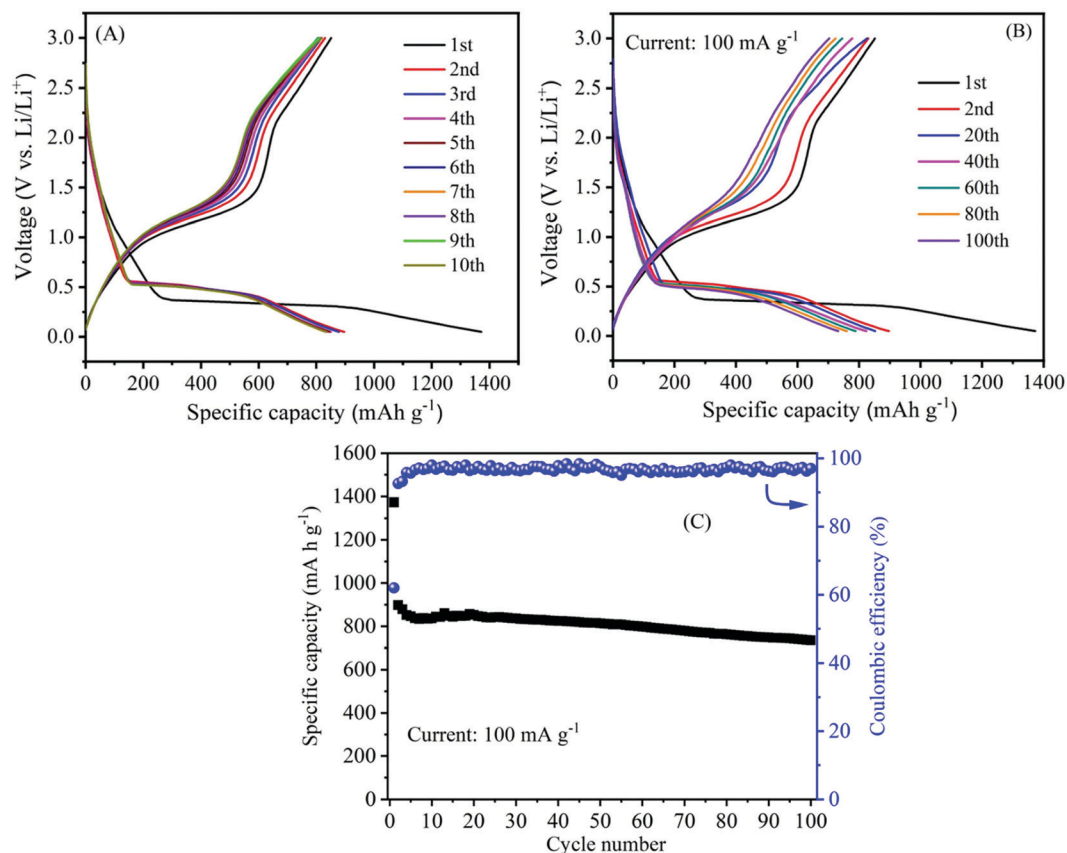
Fig. 9 Electrochemical properties of α-MnO$_2$ nanowires electrode: (A) Galvanostatic charge–discharge curves at a current density of 100 mA g^{-1} in the initial 10 cycles; (B) Typical charge–discharge curves at different cycle numbers and (C) the cycling performance (variation of the capacity with cycle number) at a current density of 100 mA g^{-1}.

reversible capacity of around 735 mA h g^{-1} was retained after 100 cycles, demonstrating an excellent cycle performance of the nanowire electrode. Meanwhile, the average Coulombic efficiency of the cell was maintained at about 97%. Moreover, the

Table 1 Comparison of the electrochemical performance of our α-MnO$_2$ hierarchical nanowires electrode with the literature reports

Synthesis method	Crystal structure	Morphology	S_{BET} (m^2 g^{-1})	1st discharge–charge capacity (mA h g^{-1})	Capacity retention (mA h g^{-1})	Rate performance (mA h g^{-1})	Ref.
Redox reaction	α-MnO$_2$	Nanoneedles	181	1373/852	735@100 cycles	495 at 1000 mA g^{-1}	This work
Low-temperature mild reduction	α-MnO$_2$	Hollow Urchins	132	746/650	481@40 cycles	—	27
Solution method	MnO$_2$/carbon nanohorns	Nanoflakes	—	1190/795	565@60 cycles	385 at 1000 mA g^{-1}	30
In situ polymerization	Birnessite-type MnO$_2$/polythiophene	Nanoneedles	136	700	500@100 cycles	—	32
Hydrothermal	Birnessite-type MnO$_2$/CNTs	Nanoflakes	—	800	600@50 cycles	310 at 4000 mA g^{-1}	52
Hydrothermal	γ-MnO$_2$	Nanocubes	—	1992/1042	602@20 cycles	—	64
Molten salt method	λ-MnO$_2$ α-MnO$_2$	Spherical Nanorods	4.7 38	1400/600 1820/910	372@50 cycles 845@50 cycles	—	65
Hydrothermal	α-MnO$_2$	Cactus-like nanostructure	75.4	196	149@25 cycles	—	66
Ultrasound irradiation	γ-MnO$_2$/CNTs	Mesoporous particles	206	1278/741	934@100 cycles	380 at 1000 mA g^{-1}	67
Hydrothermal	Birnessite-MnO$_2$	Nanosheets	—	1278/854	541@100 cycles	178 at 1000 mA g^{-1}	68
Ultra-filtration	α-MnO$_2$/graphene	Nanotubes	—	1250/686	495@40 cycles	208 at 1600 mAg^{-1}	69
In situ polymerization	MnO$_2$/Conjugated polymer/graphene	Nanorods	—	1835/1050	948@15 cycles	698 at 400 mA g^{-1}	70
Hydrothermal	α-MnO$_2$/graphene	Nanorods	149	971/483	595@60 cycles	—	71
Reflux method	α-MnO$_2$/graphene	Nanoparticles	—	1589/746	752@65 cycles	304 at 800 mA g^{-1}	72
Solvothermal	α-MnO$_2$/MWCNTs	Nanowires	—	875	770@50 cycles	—	73
Hydrothermal	Birnessite-type MnO$_2$@-carbon microbead	Flower-like texture	—	1480/698	525@100 cycles	230 at 1500 mA g^{-1}	74

performance in terms of specific capacity and stability as well as rate capability delivered by α-MnO_2 hierarchical nanowires was more significant when compared to that reported on several MnO_2 nanostructures and hybrid composites (Table 1). The excellent performance with high capacity and good cycling stability indicates considerable progress compared to other previous reports.

Besides their excellent reversible capacity and cycling stability, the prepared MnO_2 nanowire electrode also presents an impressive rate performance. Fig. 10 shows the rate capability curves (variation of the capacity as a function of applied current density) of MnO_2 nanowires. The figure clearly shows that the cell's discharge and charge capacities are gradually reduced as the applied current density increases, which is typically posed by the low diffusion rate of Li^+ ions into anodes under high current rates.[59,60] α-MnO_2 nanowires provide discharge capacities of 1369, 727, 652, 586 and 495 mA h g^{-1} at 100, 250, 500, 750 and 1000 mA g^{-1}, respectively. Even at a high applied current density of 1000 mA g^{-1}, the electrode maintained a discharge capacity of as high as 495 mA h g^{-1}. Moreover, the reversible capacity could be recovered to 890 mA h g^{-1}, when the current density reverses back to 100 mA g^{-1}, demonstrating good stability and rate capacity of α-MnO_2 nanowires.

Electrochemical impedance spectroscopy (EIS) is a powerful analytical technique widely used to analyze the electrode kinetics of α-MnO_2 material. The impedance measurements were recorded before and after cycling of the MnO_2 electrode over the frequency range of 0.01 Hz–1M Hz and 10 mV amplitude. Fig. 11 compares the Nyquist plots (real, Z' vs. imaginary, Z'') of α-MnO_2 obtained before and after 100th charge/discharge cycles. A simple equivalent circuit model (inset of Fig. 11) was built to analyze the EIS data. The Nyquist plots obtained before and after cycling are composed of a high-frequency semicircle followed by a low-frequency inclined line. The real (Z') axis intercept (at x-axis) in the high-frequency region is ascribed to Ohmic electrolyte resistance (R_s), which essentially comes from the electrolyte, electrodes, etc.[11,61] The middle-frequency region semicircle corresponds to the interface contact and the charge transfer resistance, R_{ct}.[62,63] A spike in the low-frequency region imputes
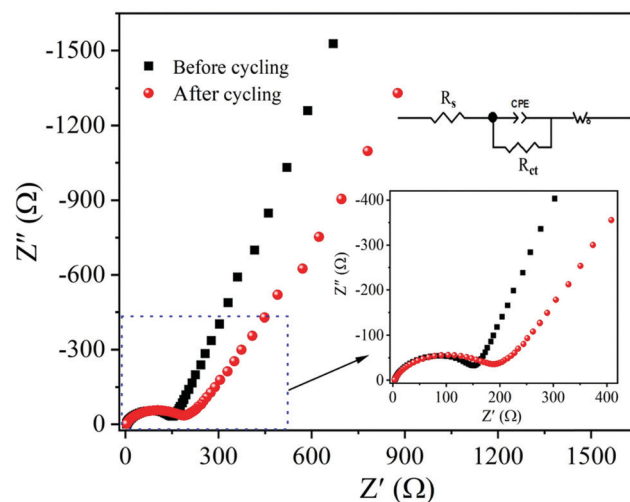

Fig. 11 EIS Nyquist plots of the α-MnO_2 nanowires electrode obtained before and after 100th charge–discharge cycles: The insets show the equivalent circuit and enlarged view of the high-frequency region.

to mass-transfer resistance. The R_{ct} value after 100 cycles is about 178 Ω, which changes only by 19.4% when compared to before cycled one, suggesting better contact between the active material and electrolyte throughout cycling, leading to better electrochemical performance of α-MnO_2 nanowires. The inclined line in the lower frequency (Warburg region) reflects the diffusion of Li^+ ions into the MnO_2 active material.[15,63]

The excellent battery performance in terms of high reversible capacity, good cycling stability and rate capability of the as-prepared α-MnO_2 can be explained as follows. First of all, hierarchical 1D nanowires with a large specific surface area and mesoporous structure can provide open channels for electrolyte penetration, thereby ensuring a good electrode/electrolyte contact area. Secondly, the nanowire architecture can relieve the stress caused by the volume change during the lithiation/delithiation and thus improve the reaction kinetics. Thirdly, the nanoscale diameter of nanowires shortens the diffusion paths for Li^+ and e^-, thus favouring fast charge transport during cycling. All these merits contributed to the fabulous electrochemical performance of α-MnO_2 nanowires, making them a promising candidate for advanced anode materials for high-performance Li-ion batteries.

4. Conclusion

We have reported a simple, inexpensive and eco-friendly approach to the synthesis of large-scale production of α-MnO_2 nanowires by a quick redox-reaction between permanganate and glycine, that was investigated as an anode material for Li-ion batteries. The unique structure of hierarchical nanowires with mesoporous structure provides high specific surface area ($\sim$181 m^2 g^{-1}) and beneficial pore-volume ($\sim$0.21 cm^3 g^{-1}). These factors are highly beneficial in energy storage applications, which allowed facile Li^+ ion transport and reinforced the electrode–electrolyte contact area during charge/
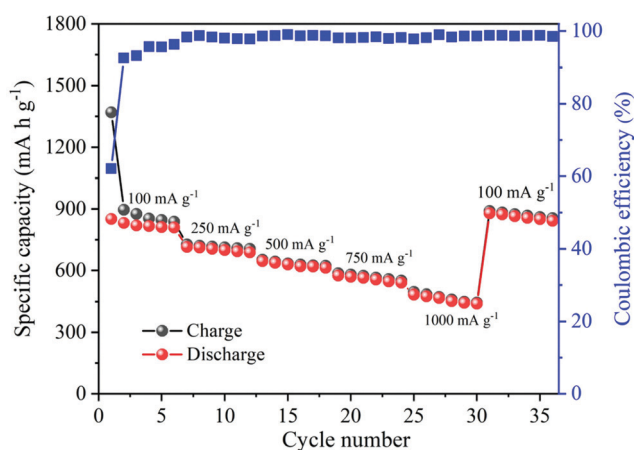

Fig. 10 The rate performance of α-MnO_2 nanowires at the rates between 100 and 1000 mA g^{-1}.

discharge cycling. As a result, a high discharge capacity of 1373 mA h g^{-1}, good rate capability, and excellent cycling performance are achieved. The electrode retained a high reversible capacity of 735 mA h g^{-1} after 100 cycles. We believe that the simple, straightforward, low-cost, and quick-redox tunable synthesis method presented here may pave the way for successfully extending the synthesis to other oxide nanostructures. These oxide nanostructures can be effectively employed for interdisciplinary energy conversion and storage applications. It can also be widely used to investigate other potential applications such as sensors, catalysis, and microelectronic devices.

Conflicts of interest

The authors declare no conflict of interest.

Acknowledgements

References

1 B. Dunn, H. Kamath and J.-M. Tarascon, *Science*, 2011, **334**, 928–935.

2 N. Nitta, F. Wu, J. T. Lee and G. Yushin, *Mater. Today*, 2015, **18**, 252–264.

3 S. Goriparti, E. Miele, F. D. Angelis, E. D. Fabrizio, R. P. Zaccaria and C. Capiglia, *J. Power Sources*, 2014, **257**, 421–443.

4 J. Wang, C. Zhang and F. Kang, *ACS Appl. Mater. Interfaces*, 2015, **7**, 9185–9194.

5 S. Konar, U. Häusserman and G. Svensson, *Chem. Mater.*, 2015, **27**, 2566–2575.

6 H. Li, W. Zhang, K. Sun, J. Guo, K. Yuan, J. Fu, T. Zhang, X. Zhang, H. Long, Z. Zhang, Y. Lai and H. Sun, *Adv. Energy Mater.*, 2021, **11**, 2100867.

7 M. V. Reddy, G. V. Subba Rao and B. V. R. Chowdari, *Chem. Rev.*, 2013, **113**, 5364–5457.

8 V. Aravindan, Y.-S. Lee and S. Madhavi, *Adv. Energy Mater.*, 2015, **5**, 1402225.

9 X. Li, D. Li, Z. Wei, X. Shang and D. He, *Electrochim. Acta*, 2014, **121**, 415–420.

10 Y. Luo, K. Wang, S. Luo, F. Zhao, H. Wu, K. Jiang, Q. Li, S. Fan and J. Wang, *ACS Appl. Nano Mater.*, 2018, **1**, 2997–3005.

11 M. V. Reddy, T. Yu, C.-H. Sow, Z. X. Shen, C. T. Lim, G. V. Subba Rao and B. V. R. Chowdari, *Adv. Funct. Mater.*, 2007, **17**, 2792–2799.

12 A. Bhaskar, M. Deepa and T. Narasinga Rao, *Nanoscale*, 2014, **6**, 10762–10771.

13 D. Li, J. Shi, H. Liu, C. Liu, G. Dong, H. Zhang, Y. Yang, G. Lu and H. Wang, *Sustainable Energy Fuels*, 2019, **3**, 1055–1065.

14 M. S. Salman, A. R. Park, M. J. Cha, Y. Choi, S. K. Jang, L. Tan, P. J. Yoo and W. S. Choe, *ACS Appl. Nano Mater.*, 2018, **1**, 698–710.

15 A. Bhaskar, M. Deepa and T. Narasinga Rao, *ACS Appl. Mater. Interfaces*, 2013, **5**, 2555–2566.

16 P. Poizot, S. Laruelle, S. Grugeon, L. Dupont and J.-M. Tarascon, *Nature*, 2000, **407**, 496–499.

17 P. K. Nayak, T. R. Penki and N. Munichandraiah, *J. Electroanal. Chem.*, 2013, **703**, 126–134.

18 Y. Li, Q. Zhang, J. Zhu, X.-L. Wei and P. K. Shen, *J. Mater. Chem. A*, 2014, **2**, 3163–3168.

19 Y. Deng, L. Wan, Y. Xie, X. Qin and G. Chen, *RSC Adv.*, 2014, **4**, 23914–23935.

20 J. Huang, L. M. Housel, C. D. Quilty, A. B. Brady, P. F. Smith, A. Abraham, M. R. Dunkin, D. M. Lutz, B. Zhang, E. S. Takeuchi, A. C. Marschilok and K. J. Takeuchi, *J. Electrochem. Soc.*, 2018, **165**, A2849–A2858.

21 E. Umeshbabu, P. Justin and G. Ranga Rao, *ACS Appl. Energy Mater.*, 2018, **1**, 3654–3664.

22 Y. S. Yun, J. M. Kim, H. H. Park, J. Lee, Y. S. Huh and H.-J. Jin, *J. Power Sources*, 2013, **244**, 747–751.

23 C. Guo, H. Liu, J. Li, Z. Hou, J. Liang, J. Zhou, Y. Zhu and Y. Qian, *Electrochim. Acta*, 2019, **304**, 370–377.

24 C. S. Johnson, M. F. Mansuetto, M. M. Thackeray, Y. Shao-Horn and S. A. Hackney, *J. Electrochem. Soc.*, 1997, **144**, 2279–2282.

25 Y. Tang, S. Zheng, Y. Xu, X. Xiao, H. Xue and H. Pang, *Energy Storage Mater.*, 2018, **12**, 284–309.

26 S. Liu, X. Liu, J. Zhao, Z. Tong, J. Wang, X. Ma, C. Chi, D. Su, X. Liu and Y. Li, *RSC Adv.*, 2016, **6**, 85222–85229.

27 B. Li, G. Rong, Y. Xie, L. Huang and C. Feng, *Inorg. Chem.*, 2006, **45**, 6404–6410.

28 J. Chen, Y. Wang, X. He, S. Xu, M. Fang, X. Zhao and Y. Shang, *Electrochim. Acta*, 2014, **142**, 152–156.

29 Y. Li, D. Ye, B. Shi, W. Liu, R. Guo, H. Pei and J. Xie, *Phys. Chem. Chem. Phys.*, 2017, **19**, 7498–7505.

30 H. Lai, J. Li, Z. Chen and Z. Huang, *ACS Appl. Mater. Interfaces*, 2012, **4**, 2325–2328.

31 A. L. Mohana Reddy, M. M. Shaijumon, S. R. Gowda and P. M. Ajayan, *Nano Lett.*, 2009, **9**, 1002–1006.

32 W. Xiao, J. S. Chen, Q. Lu and X. W. Lou, *J. Phys. Chem. C*, 2010, **114**, 12048–12051.

33 S. Bose, T. Kuila, A. K. Mishra, N. H. Kim and J. H. Lee, *J. Mater. Chem.*, 2012, **22**, 9696.

34 S. Bag and C. R. Raj, *J. Mater. Chem. A*, 2016, **4**, 8384–8394.

35 K. J. M. Bishop, C. E. Wilmer, S. Soh and B. A. Grzybowski, *Small*, 2009, **5**, 1600–1630.

36 A. K. Pearce, T. R. Wilks, M. C. Arno and R. K. O'Reilly, *Nat. Rev. Chem.*, 2020, **21**, 21–45.

37 M. Grzelczak, J. Vermant, E. M. Furst and L. M. Liz-Marzán, *ACS Nano*, 2010, **4**, 3591–3605.

38 M. H. Rossouw, D. C. Liles, M. M. Thackeray, W. I. F. David and S. Hull, *Mater. Res. Bull.*, 1992, **27**, 221–230.

39 L. Li, Y. Pan, L. Chen and G. Li, *J. Solid State Chem.*, 2007, **180**, 2896–2904.

40 I. I. Misnon, R. A. Aziz, N. K. M. Zain, B. Vidhyadharan, S. G. Krishnan and R. Jose, *Mater. Res. Bull.*, 2014, **57**, 221–230.

41 H. T. Zhu, J. Luo, H. X. Yang, J. K. Liang, G. H. Rao, J. B. Li and Z. M. Du, *J. Phys. Chem. C*, 2008, **112**, 17089–17094.

42 E. Eren, H. Gumus and A. Sarihan, *Desalination*, 2011, **279**, 75–85.

43 H. Huang, G. Sun, J. Hu and T. Jiao, *J. Chem.*, 2015, **8**, 629362.

44 W. Li, X. Cui, R. Zeng, G. Du, Z. Sun, R. Zheng, S. P. Ringer and S. X. Dou, *Sci. Rep.*, 2015, **5**, 8987.

45 A. M. Hashem, H. Abuzeid, M. Kaus, S. Indris, H. Ehrenberg, A. Mauger and C. M. Julien, *Electrochim. Acta*, 2018, **262**, 74–81.

46 S. Liang, F. Teng, G. Bulgan, R. Zong and Y. Zhu, *J. Phys. Chem. C*, 2008, **112**, 5307–5315.

47 W. Li, J. Liu and D. Zhao, *Nat. Rev. Mater.*, 2016, **1**, 16023.

48 Y. Ren, Z. Ma, R. E. Morris, Z. Liu, F. Jiao, S. Dai and P. G. Bruce, *Nat. Commun.*, 2013, **4**, 2015.

49 X. Guo, J. Han, L. Zhang, P. Liu, A. Hirata, L. Chen, T. Fujita and M. Chen, *Nanoscale*, 2015, **7**, 15111–15116.

50 M. Toupin, T. Brousse and D. Bélanger, *Chem. Mater.*, 2004, **16**, 3184–3190.

51 J. Deng, L. Chen, Y. Sun, M. Ma and L. Fu, *Carbon*, 2015, **92**, 177–184.

52 H. Xia, M. Lai and L. Lu, *J. Mater. Chem.*, 2010, **20**, 6896–6902.

53 H. Kim, N. Venugopal, J. Yoon and W.-S. Yoon, *J. Alloys Compd.*, 2019, **778**, 37–46.

54 S. Z. Huang, Y. Cai, J. Jin, J. Liu, Y. Li, H.-E. Wang, L.-H. Chen, T. Hasan and B. L. Su, *J. Mater. Chem. A*, 2016, **4**, 4264–4272.

55 Z. Li, J. Wang, Z. Wang, Y. Tang, C.-S. Lee and S. Yang, *RSC Adv.*, 2014, **4**, 54416–54421.

56 J. Yoon, W. Choi, T. Kim, H. Kim, Y. S. Choi, J. M. Kim and W.-S. Yoon, *J. Energy Chem.*, 2021, **53**, 276–284.

57 R. Cai, S. Guo, Q. Meng, S. Yang, H. L. Xin, X. Hu, M. Li, Y. Sun, P. Gao, S. Zhang, H. Dong, S. Lei, K. Kim, H. Zeng, L. Sun, F. Xu and Y. Zhu, *Nano Energy*, 2019, **63**, 103840.

58 J. Chen, Y. Wang, X. He, S. Xu, M. Fang, X. Zhao and Y. Shang, *Electrochim. Acta*, 2014, **142**, 152–156.

59 N. Zhao, S. Wu, C. He, Z. Wang, C. Shi, E. Liu and J. Li, *Carbon*, 2013, **57**, 130–138.

60 J. H. Park, W. Y. Choi, S. Lee, T.-S. Kim and J. W. Lee, *Electrochim. Acta*, 2020, **348**, 136310.

61 M. Satyanarayana, A. K. Jibin, E. Umeshbabu1, J. James and U. V. Varadaraju, *Ionics*, DOI: 10.1007/s11581-021-04297-2.

62 Y. Hu, K. Wu, F. Zhang, H. Zhou and L. Qi, *ACS Appl. Nano Mater.*, 2019, **2**, 429–439.

63 Y. Yang, G. Ma, J. Huang, J. Nan, S. Zhen, Y. Wang and A. Li, *J. Solid State Chem.*, 2020, **286**, 121297.

64 J. Zhao, Z. Tao, J. Liang and J. Chen, *Cryst. Growth Des.*, 2008, **8**, 2799–2805.

65 P. Nithyadharseni, M. V. Reddy, H. Fanny, S. Adams and B. V. R. Chowdari, *RSC Adv.*, 2015, **5**, 60552–60561.

66 R. Rajagopal and K.-S. Ryu, *J. Energy Storage*, 2020, **32**, 101880.

67 Y. S. Yun, J. M. Kim, H. H. Park, J. Lee, Y. S. Huh and H.-J. Jin, *J. Power Sources*, 2013, **244**, 747–751.

68 Y. Wang, Z. Han, S. Yu, R. Song, H. Song, K. Ostrikov and H. Yang, *Carbon*, 2013, **64**, 230–236.

69 A. Yu, H. W. Park, A. Davies, D. C. Higgins, Z. Chen and X. Xiao, *J. Phys. Chem. Lett.*, 2011, **2**, 1855–1860.

70 C. Xian Guo, M. Wang, T. Chen, X. W. Lou and C. Ming Li, *Adv. Energy Mater.*, 2011, **1**, 736–741.

71 H. Liu, Z. Hu, Y. Su, H. Ruan, R. Hu and L. Zhang, *Appl. Surf. Sci.*, 2017, **392**, 777–784.

72 K. Wen, G. Chen, F. Jiang, X. Zhou and J. Yang, *Int. J. Electrochem. Sci.*, 2015, **10**, 3859–3866.

73 S. J. Ee, H. Pang, U. Mani, Q. Yan, S. L. Ting and P. Chen, *ChemPhysChem*, 2014, **15**, 2445–2449.

74 H. Wang, J. Liu, X. Wang, C. Wu, Q. Zhao, Y. Fu, X. Yang and H. Shu, *RSC Adv.*, 2014, **4**, 22241–22245.